


Nodal-line semimetal HMTSF-TCNQ: Anomalous orbital diamagnetism and charge density waveS. Ozaki^{1,*}, I. Tateishi^{1,2}, H. Matsuura¹, M. Ogata^{1,3}, and K. Hiraki^{4,5}¹*Department of Physics, University of Tokyo, Bunkyo, Tokyo 113-0033, Japan*²*RIKEN Center for Emergent Matter Science, Wako, Saitama 351-0198, Japan*³*Trans-scale Quantum Science Institute, University of Tokyo, Bunkyo, Tokyo 113-0033, Japan*⁴*Department of Natural Science, Fukushima Medical University, Fukushima 960-1295, Japan*⁵*IMR, Tohoku University, Miyagi 980-8577, Japan* (Received 14 June 2021; revised 27 August 2021; accepted 28 September 2021; published 25 October 2021)

This study investigates the electronic states and physical quantities of an organic charge-transfer complex HMTSF-TCNQ, which undergoes a charge-density-wave (CDW) phase transition at temperature $T_c \simeq 30$ K. A first-principles calculation is utilized to determine that the normal state is a topological semimetal with open nodal lines. Based on the first-principles calculation, we develop a tight-binding model to investigate the electronic state in detail. Below T_c , the CDW phase is examined in the tight-binding scheme using the mean-field approximation. It is shown that the open nodal lines are deformed into closed ones, and their shapes are sensitive to the order parameter. Using this tight-binding model, we theoretically evaluate the temperature dependencies of two physical quantities: the spin-lattice relaxation time T_1 and the orbital magnetic susceptibility. In particular, an anomalous plateau is obtained at low temperatures in the orbital diamagnetism. We conclude that this anomalous plateau originates owing to the conflict between the interband diamagnetism, impurity scattering, and the nodal-line deformation. We also conduct an experiment to investigate the orbital magnetism, and the results are in excellent quantitative agreement with the theory.

DOI: [10.1103/PhysRevB.104.155202](https://doi.org/10.1103/PhysRevB.104.155202)**I. INTRODUCTION**

A charge density wave (CDW) in topological bands induces fascinating phenomena, such as the three-dimensional Hall effect [1] and axionic CDW phase [2], which have recently generated considerable research interest. A CDW is a quantum phase that is typical of quasi-one-dimensional organic conductors, and the topological properties of organic materials have become more extensively researched in the last two decades [3–11]. Organic materials that possess topological properties have the potential for novel phenomena that originate from the interplay between their topological bands and the CDW. Such materials require both one dimensionality for the CDW and two or three dimensionality for the topological nature. One example of these materials is HMTSF-TCNQ (hexamethylene-tetraselena-fulvalene-tetracyanoquinodimethane) [12–15].

HMTSF-TCNQ is a classical quasi-one-dimensional charge-transfer complex that was discovered in the 1970s, and it has attracted considerable attention in contemporary research, owing to the possibility of field-induced CDW [16–18]. HMTSF-TCNQ has components that are similar to those of the well-known organic complexes TTF-TCNQ and TMTSF₂PF₆, which are known as a typical organic conductor that has a CDW and the first organic superconductor identified, respectively [19,20]. These two materials have been studied extensively; however, HMTSF-TCNQ has not.

HMTSF-TCNQ undergoes a CDW transition at approximately 30 K under ambient pressure; however, the tem-

perature dependence of the resistivity is different from that of TTF-TCNQ in that a clear metal-insulator transition is not observed. According to Refs. [15,19], the Fermi surface of HMTSF-TCNQ is two dimensional, owing to the relatively large interchain hoppings, which causes incomplete CDW nesting. In this material, unconventional temperature dependencies of physical quantities, such as the magnetic susceptibility [14], Seebeck coefficient [12], and the electric conductivity are known and are expected to be attributed to the incomplete CDW nesting.

Despite these intriguing properties, there are no reliable theoretical models for the electronic states of the normal phase or the CDW phase. The electronic state of the normal phase is typically discussed in terms of Weger's model [15], which is a four-band tight-binding model that consists of HOMOs (highest occupied molecular orbitals) and LUMOs (lowest unoccupied molecular orbitals) for each molecule on the basis of the crystal structure known at that time with the estimated hopping parameters. This model was able to explain some experimental results; however, a subsequent experimental study suggested the crystal structure of a different space group [21]. Furthermore, the first-principles calculation based on the new crystal structure, which is presented in this study, suggests Fermi surfaces of different shapes and locations from those calculated by Weger. Therefore, we need to modify the existing model on the basis of these results.

The physical quantities of HMTSF-TCNQ are of interest as well as its electronic states. In particular, HMTSF-TCNQ shows a large diamagnetism at low temperatures, and it reaches an anomalous plateau below T_c [14]. Weger tried to explain this behavior via his model and concluded that the diamagnetism was attributed to Landau diamagnetism.

*ozaki@hosi.phys.s.u-tokyo.ac.jp

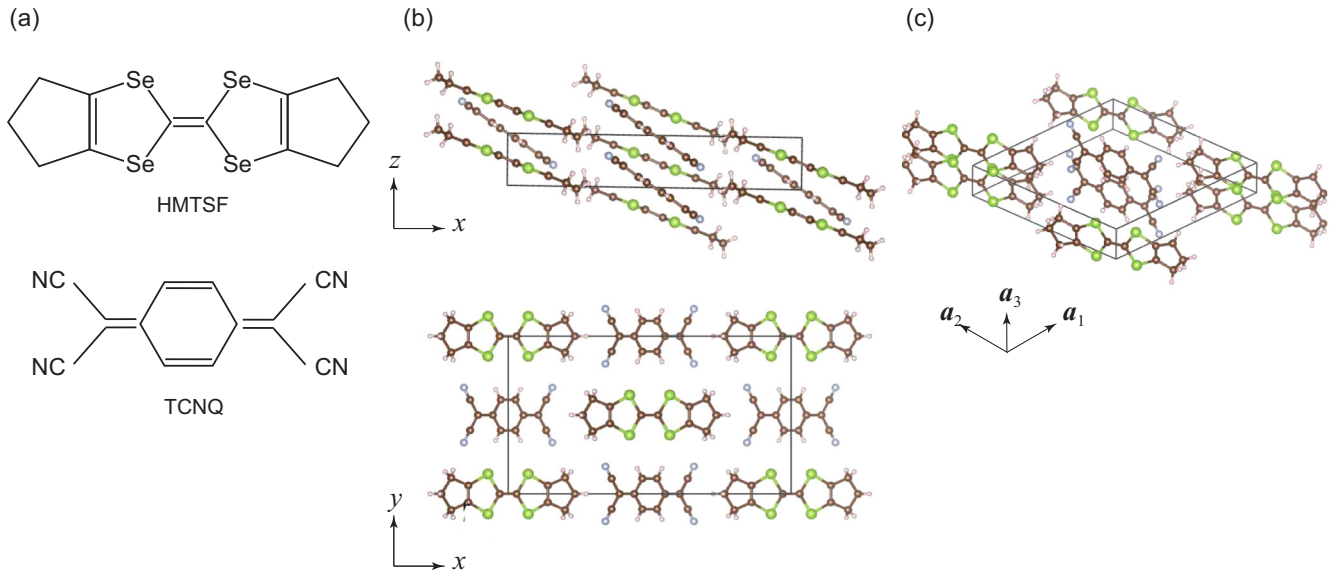


FIG. 1. (a) Molecular structures of HMTSF and TCNQ. (b) Conventional and (c) primitive cell of HMTSF-TCNQ. Brown, green, blue, and white circles represent C, Se, N, and H atoms, respectively. The black lines represent the boundary of each unit cell. The primitive cell is half the size of the conventional cell.

However, this claim is debatable because Landau diamagnetism is derived from the electrons on the Fermi surface. In the CDW state, the density of states (DOS) at the Fermi level is expected to be small. Therefore, Landau diamagnetism does not explain the large diamagnetism at low temperatures; thus, the origin of the diamagnetism remains unknown.

To address these problems, the current study serves a twofold purpose. One is to reveal the electronic states of the normal and CDW phases of HMTSF-TCNQ under ambient pressure. First, we perform a first-principles calculation. The obtained results, in particular the symmetry indicator, indicate that its normal phase is a topologically protected nodal-line semimetal. On the basis of these results, we construct a tight-binding model and discuss the nodal lines in detail. These analyses clarify that the energy at the node points fluctuate along the nodal lines, which results in electron and hole pockets. As a result, we expect that the nodal lines influence various physical quantities that are susceptible to the Fermi surface. Furthermore, assuming a plausible CDW nesting, we discuss how the CDW affects the nodal lines and the electron and hole pockets. We theoretically evaluate the spin-lattice relaxation time T_1 for the experimental confirmation of the existence of the nodal lines.

The other objective is to clarify the derivation of the large diamagnetism and its temperature dependence. Since the nodal lines are located near the Fermi level, a large diamagnetism derived from the interband effect is strongly expected from an analogy to the case of the Dirac electrons [22–28]. Note that the interband effect is insensitive to the DOS at the Fermi level. Using the Fukuyama formula [29], which properly describes the interband effect, we evaluate the magnetic susceptibility. An experiment is conducted to determine the magnetic susceptibility using a superconducting quantum interference device (SQUID) magnetometer. The proposed theory is in excellent agreement with this experimental result.

This paper is organized as follows. In Sec. II the correct crystal structure of HMTSF-TCNQ is presented. In Sec. III we investigate the electronic state of HMTSF-TCNQ using the first-principles calculation, and we demonstrate the existence of nodal lines. In Sec. IV we construct a tight-binding model based on the results of the previous section and discuss the nodal lines in detail. In Sec. V we introduce the CDW with the mean-field approximation and examine the CDW phase. In Sec. VI we evaluate the spin-lattice relaxation time T_1 and the orbital magnetic susceptibility. A comparison between the theory and the magnetic susceptibility experimental results is also conducted. Finally, we present the conclusion to the study in Sec. VII.

II. CRYSTAL STRUCTURE OF HMTSF-TCNQ

HMTSF-TCNQ consists of two organic molecules, HMTSF and TCNQ, the structure of which are shown in Fig. 1(a). This material has a base-centered monoclinic lattice, and for convenience, we introduce two different notations of the unit cell: The conventional cell and the primitive cell, which are shown in Figs. 1(b) and 1(c), respectively. The crystal structures and wave functions in this study are drawn using VESTA (JP minerals, Japan) [30]. Each molecule forms a one-dimensional chain, and the HMTSF and TCNQ chains are arranged in a checkerboard configuration, as can be observed in Fig. 1(b). Throughout this study we use the Cartesian coordinate system, as shown in Fig. 2(a) (the unique axis b convention). The space group is $C2/m$ (No. 12), the generators of which are lattice translations, C_{2y} rotation, and inversion I [31]. In the following we will compare the theoretical calculation with experimental results obtained in a recently synthesized sample [32]. The lattice constants for this sample at room temperature are tabulated in Table I, which are in good agreement with those obtained in a previous study [21]. The experimental details will be presented elsewhere

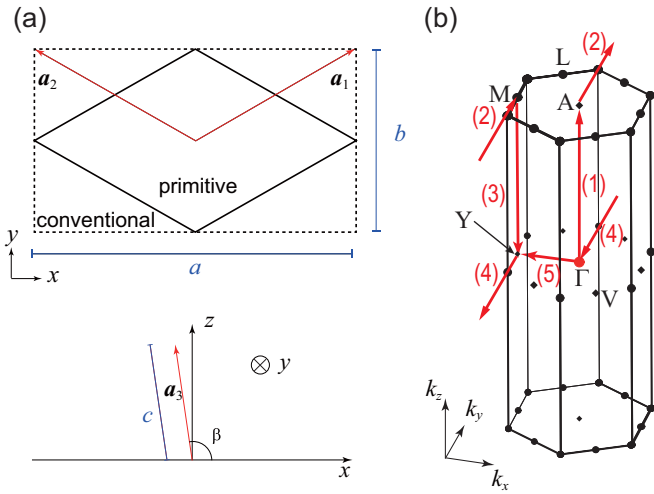


FIG. 2. (a) Basic lattice vectors for the primitive cell of HMTSF-TCNQ. The rhombus and dashed rectangle represent the boundary of the primitive and conventional cell, respectively. The lattice constants a , b , c , and β are for the conventional cell. (b) First Brillouin zone and TRIM. The TRIM are Γ , A, Y, M, two V, and two L points. The path for the energy dispersion is also shown.

[33]. For comparison between theory and experiments, we use the former lattice constants for theoretical analyses.

Figure 2(a) shows the basic lattice vectors for the primitive cell, $\mathbf{a}_1 = (a/2, b/2, 0)$, $\mathbf{a}_2 = (-a/2, b/2, 0)$, and $\mathbf{a}_3 = (c \cos \beta, 0, c \sin \beta)$. The orientation of the chains are parallel to \mathbf{a}_3 , and the corresponding reciprocal lattice vectors are $\mathbf{b}_1 = 2\pi(1/a, 1/b, -1/a \tan \beta)$, $\mathbf{b}_2 = 2\pi(-1/a, 1/b, 1/a \tan \beta)$, and $\mathbf{b}_3 = 2\pi(0, 0, 1/c \sin \beta)$. Note that \mathbf{a}_3 is almost parallel to the z axis, but slightly inclined towards the negative x direction and that \mathbf{b}_3 is parallel to the k_z axis. Figure 2(b) shows the first Brillouin zone, which is a hexagonal column, and the time-reversal invariant momenta (TRIM) are Γ , A, Y, M, two V, and two L points.

III. FIRST-PRINCIPLES CALCULATION OF HMTSF-TCNQ

In this section we present the electronic state of HMTSF-TCNQ, obtained by a first-principles calculation. This calculation is performed by QUANTUM ESPRESSO [34], which uses the density functional theory [35,36]. We neglect spin-orbit interaction (SOI) because in organic materials it is typically negligible. For the exchange-correlation term, the generalized gradient approximation with nonrelativistic Perdew-Burke-Ernzerhof parametrization [37] is used. The Kohn-Sham orbitals are expanded with plane waves and the cutoff energies are 70 and 320 Ry for wave functions and charge density, respectively. (The cutoff stability is discussed in Appendix A.) The \mathbf{k} -point grid on the Brillouin zone is

TABLE I. Lattice constants for the conventional cell.

	$a/\text{\AA}$	$b/\text{\AA}$	$c/\text{\AA}$	β/deg
Present [32]	21.85(4)	12.48(2)	3.871(7)	90.25(3)
Ref. [21]	21.999(14)	12.573(8)	3.890(1)	90.29(4)

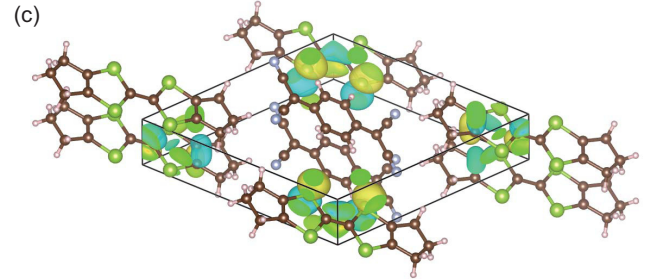
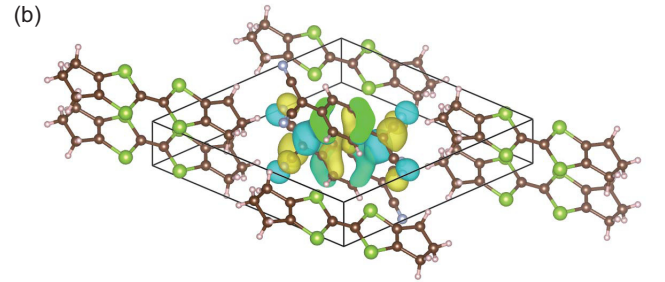
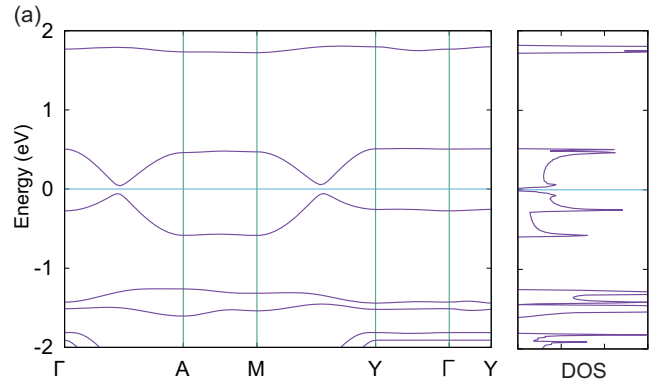


FIG. 3. (a) Energy dispersion and DOS of HMTSF-TCNQ. Wave functions for (b) valence and (c) conduction bands at the Γ point. These wave functions consist of two Wannier functions, which are the same for wave functions at other high-symmetry points, shown in Appendix B.

taken as $8 \times 8 \times 40$. The obtained energy dispersion and DOS are shown in Fig. 3(a), and the corresponding path is shown in Fig. 2(b). First, we find that the dispersion is almost flat in the k_x and k_y directions, and the DOS has peaks at the band edges. These properties are characteristic of quasi-one-dimensional materials. Another important feature is that the two bands near the Fermi level are very isolated from other bands. This implies that the mixing of other orbitals is small and that it is sufficient to consider these two bands to discuss the low-energy properties of this material. An energy gap is observed in the energy dispersion at the Fermi energy in Fig. 3(a); however, the DOS does not show a clear gap. As shown below, this is because there are nodal lines away from the high-symmetry \mathbf{k} points. This Dirac-type dispersion may strongly affect physical quantities, such as the orbital diamagnetism.

Next, we examine the spatial distribution of the wave functions. Figures 3(b) and 3(c) show the wave functions at the

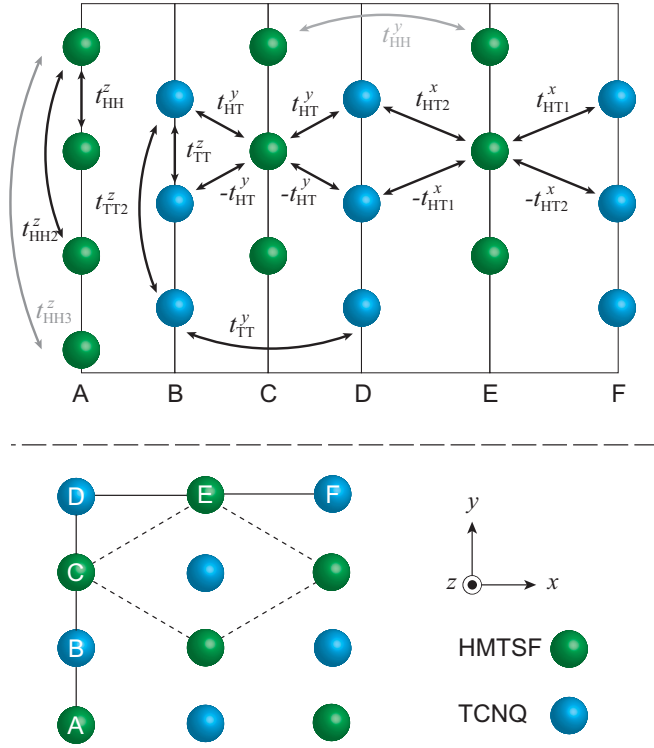


FIG. 4. Eight largest hopping parameters used in the tight-binding model [Eq. (6)]. The subscript and superscript represent the related molecules and the direction of the hopping, respectively. The hoppings t_{HH3}^z and t_{HH}^y are shown for comparison and are not used in the present study. The lower panel shows the configuration of the molecules viewed from the z direction, and A–F indicate the positions of atoms in the upper panel. The dashed line represents the primitive unit cell.

Γ point for the valence and conduction bands, respectively. We observe that the wave functions at other high-symmetry points also consist of these two Wannier functions. (The wave functions at other high-symmetry points are shown in Appendix B.) Therefore, we can naturally assume that the two bands at each \mathbf{k} point are well described by the linear combination of these two Wannier functions.

Third, we discuss the topological nature of the material using the symmetry indicator. We can observe that there is no band crossing on the high-symmetry lines or planes. However, the space group No. 12 can have nodal lines at generic points [38–41]. The existence of nodal lines is diagnosed by the symmetry indicator $(z_{2,2}, z'_2)$, the components of which are defined by

$$z_{2,2} = \sum_{\mathbf{k}=\text{V,Y,M,L}} n^-(\mathbf{k}) \pmod{2}, \quad (1)$$

$$z'_2 = \frac{1}{2} \sum_{\mathbf{k}=\text{8TRIM}} n^-(\mathbf{k}) \pmod{2}, \quad (2)$$

where $n^-(\mathbf{k})$ is the number of occupied bands with odd parity at \mathbf{k} . This indicator is calculated by examining the parities of the wave functions, and we obtain a nontrivial indicator $(z_{2,2}, z'_2) = (1, 1)$. This value indicates the existence of open nodal lines approximately along the k_x direction [42]. (The parities at TRIM are shown in Appendix B.)

TABLE II. One-body levels and hopping parameters between Wannier functions. Hoppings whose absolute values are less than $|t_{TT}^y|$ are neglected.

Parameters	Energy / eV
ε_T	0.0542
ε_H	−0.0316
t_{HH}^z	0.269
t_{TT}^z	−0.184
t_{HT}^y	0.0193
t_{TT2}^z	0.0126
t_{HH2}^z	0.0106
t_{HT1}^x	−0.00689
t_{HT2}^x	0.00446
t_{TT}^y	−0.00358
t_{HH3}^z	0.00207
t_{HH}^y	−0.00202
\vdots	\vdots

IV. TIGHT-BINDING MODEL AND NODAL LINES

A. Tight-binding model

In the previous section the discussion based on the symmetry indicator suggests the existence of the nodal lines. However, the symmetry indicator does not indicate their exact locations or detailed properties. Therefore, we construct a tight-binding model and analyze it to clarify the detailed electronic properties.

As shown in the previous section, the wave functions near the Fermi level consist of the two Wannier functions located in HMTSF and TCNQ molecules. From these orbitals we construct a two-band tight-binding model using Slater-Koster's method [43]. We fit the hopping parameters to reproduce the band dispersion using WANNIER90 [44]. From this result we consider the eight largest hopping parameters and neglect the others. The chosen hoppings are shown in Fig. 4, and the fitted parameters are summarized in Table II. We measure the energies from the Fermi level (i.e., $\mu = 0$) and denote the one-body level for the HMTSF (TCNQ) orbital as ε_H (ε_T). Using the Fourier transform, we obtain the two-band tight-binding model in the \mathbf{k} space as follows:

$$H_0(\mathbf{k}) = \begin{pmatrix} t_{HH}(\mathbf{k}) & t_{HT}^*(\mathbf{k}) \\ t_{HT}(\mathbf{k}) & t_{TT}(\mathbf{k}) \end{pmatrix}, \quad (3)$$

where

$$t_{HH}(\mathbf{k}) = \varepsilon_H + 2t_{HH}^z \cos \tilde{k}_z c + 2t_{HH2}^z \cos 2\tilde{k}_z c, \quad (4)$$

$$t_{TT}(\mathbf{k}) = \varepsilon_T + 2t_{TT}^z \cos \tilde{k}_z c + 2t_{TT2}^z \cos 2\tilde{k}_z c + 2t_{TT}^y \cos k_y b, \quad (5)$$

$$t_{HT}(\mathbf{k}) = 4it_{HT}^y \cos \frac{k_y b}{2} \sin \frac{\tilde{k}_z c}{2} + 2it_{HT1}^x \sin \left(-\frac{k_x a}{2} + \frac{\tilde{k}_z c}{2} \right) + 2it_{HT2}^x \sin \left(\frac{k_x a}{2} + \frac{\tilde{k}_z c}{2} \right), \quad (6)$$

with $\tilde{k}_z = k_x \cos \beta + k_z \sin \beta$.

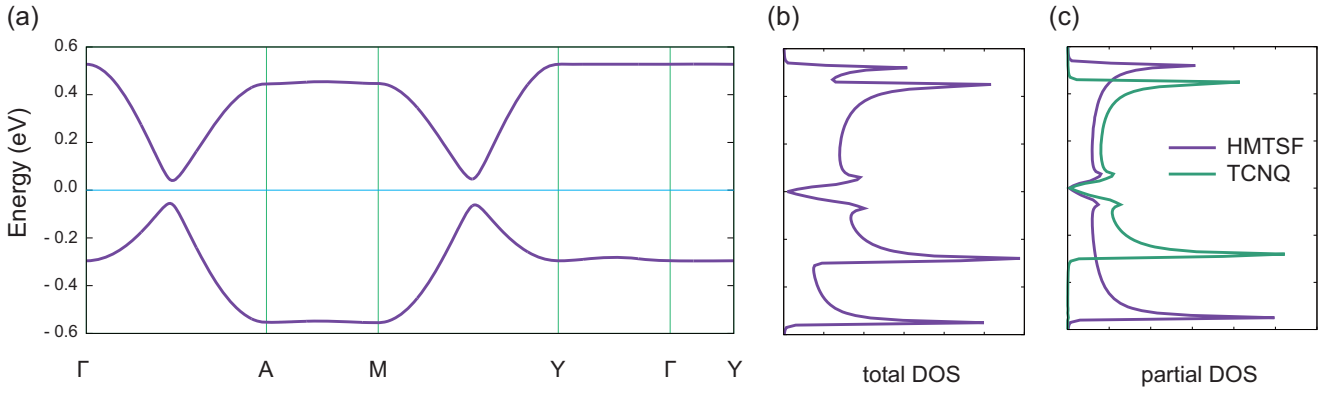


FIG. 5. (a) Energy dispersion and (b) the total DOS of the proposed tight-binding model. (c) Partial DOS for HMTSF and TCNQ.

Diagonalizing the Hamiltonian in Eq. (3), we obtain the energy dispersion:

$$E_{\pm} = \frac{t_{\text{HH}}(\mathbf{k}) + t_{\text{TT}}(\mathbf{k})}{2} \pm \sqrt{|t_{\text{HT}}(\mathbf{k})|^2 + \frac{1}{4}[t_{\text{HH}}(\mathbf{k}) - t_{\text{TT}}(\mathbf{k})]^2}, \quad (7)$$

which is shown in Fig. 5(a). The total DOS is shown in Fig. 5(b). These results accurately reproduce those by the first-principles calculation shown in Fig. 3(a). In the DOS we observe a linear behavior near the Fermi level, which is typical for two-dimensional Dirac electrons. Figure 5(c) shows the partial DOS for HMTSF and TCNQ molecules. While these wave functions decouple at the band edge, they contribute almost equally to the DOS at the Fermi level. This result supports the existence of the Dirac-type dispersion, because it always consists of at least two orbitals. The shape of the Dirac cone calculated from the proposed tight-binding model is shown in Appendix C.

B. Nodal lines

This subsection discusses the locations of the nodal lines in the \mathbf{k} space. From the energy dispersion Eq. (7), we can identify the nodal lines by the following condition:

$$t_{\text{HT}}(\mathbf{k}) = 0, \quad t_{\text{HH}}(\mathbf{k}) = t_{\text{TT}}(\mathbf{k}). \quad (8)$$

Solving Eq. (8) numerically, we obtain the configuration of the nodal lines as shown in Figs. 6(a) and 6(b). The bird's eye view [Fig. 6(a)] indicates that the nodal lines are approximately along the k_x direction, as discussed in Sec. III, and are almost located on the planes perpendicular to the k_z axis. Because the crystal has C_{2y} rotation, inversion, and σ_y symmetries, the nodal lines have the same symmetries. In particular, owing to the C_{2y} rotation symmetry, the projection of the nodal lines onto the k_x - k_y plane [Fig. 6(b)] intersect on the $k_x = 0$ line. Figure 6(c) shows the Fermi surface of the proposed tight-binding model, where the purple and green surfaces represent the electron and hole pockets, respectively. The energy at the Dirac node point fluctuates along the nodal lines, which results in alternating thin tube-shaped electron and hole pockets.

V. CDW PHASE

HMTSF-TCNQ exhibits a CDW phase transition at $T_c \simeq 30$ K. Theoretically, the nesting vector of this CDW state is presumed to be the vector between Dirac points on the nodal lines at the Fermi level, as shown in Fig. 6(a). In the proposed model, the nesting vector is $\mathbf{q} \simeq (0, 0, 0.937\pi/c \cos \beta)$. Although the obtained nesting vector is slightly different from the experimental value [45] $\mathbf{q} \simeq (0, 0, 0.74\pi/c \cos \beta)$, we use the former in the following analyses.

Considering the nesting in the mean-field approximation [46–48], the effective model becomes

$$H_{\text{CDW}}(\mathbf{k}) = \begin{pmatrix} t_{\text{HH}}(\mathbf{k}) & t_{\text{HT}}^*(\mathbf{k}) & \Delta & 0 \\ t_{\text{HT}}(\mathbf{k}) & t_{\text{TT}}(\mathbf{k}) & 0 & \Delta \\ \Delta & 0 & t_{\text{HH}}(\mathbf{k} - \mathbf{q}) & t_{\text{HT}}^*(\mathbf{k} - \mathbf{q}) \\ 0 & \Delta & t_{\text{HT}}(\mathbf{k} - \mathbf{q}) & t_{\text{TT}}(\mathbf{k} - \mathbf{q}) \end{pmatrix}, \quad (9)$$

where Δ is the order parameter of the CDW state, which is assumed to be common in the HMTSF and TCNQ chain for simplicity. Note that the periodicity in the k_z direction is lost and that k_z is only allowed in the vicinity of the nodal lines in the $k_z > 0$ region ($k_z \simeq 0.38 \text{ \AA}^{-1}$). However, the nodal lines are located on almost the same plane as in the case of $\Delta = 0$; therefore, we can still discuss the nodal lines using the effective Hamiltonian in Eq. (9).

Diagonalizing the effective model of Eq. (9), we obtain the Δ dependence of the nodal lines, as shown in Fig. 7(a). The blue, orange, and green lines represent the nodal lines with $\Delta = 5, 10,$ and 15 meV, respectively. For the case of $\Delta = 0$ meV [Fig. 6(b)], the nodal lines touch each other at a point. However, with finite Δ , a band gap opens at this point, which is connected by the nesting vector. As a result, closed nodal lines are formed. As Δ increases, the closed nodal lines become small and vanish when $\Delta \simeq 18$ meV. Figures 7(b) and 7(c) show the Fermi surfaces for the cases with $\Delta = 5$ meV and $\Delta = 10$ meV, respectively. They consist of alternating electron and hole pockets along the nodal lines, as in the case of $\Delta = 0$ meV, and these CDW states are still semimetallic.

VI. PHYSICAL QUANTITIES

In this section we evaluate two physical quantities that are important to the experiments: the spin-lattice relaxation time T_1 and orbital magnetic susceptibility.

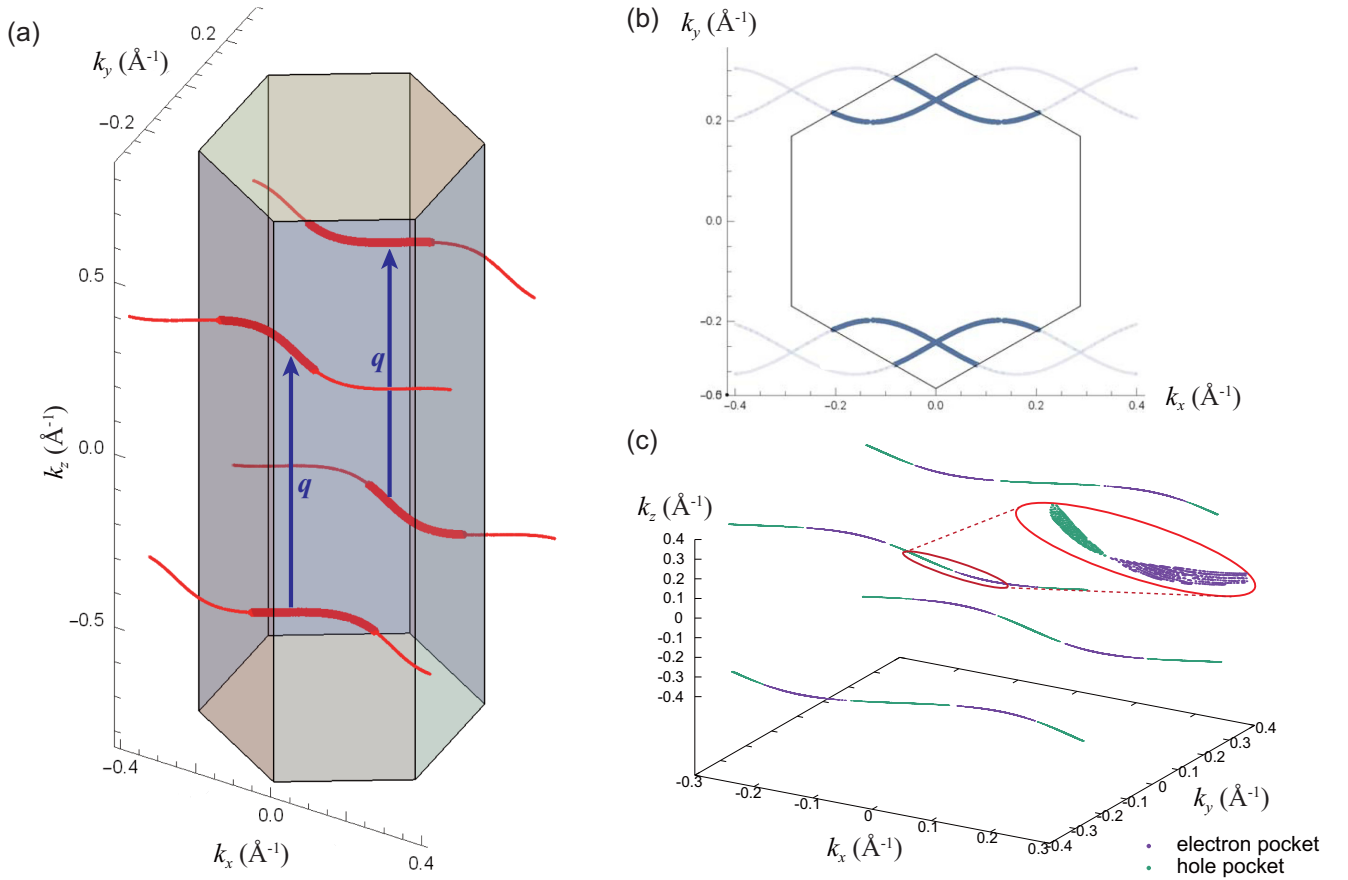


FIG. 6. (a) Configuration of the nodal lines in the k space. The nodal lines in (out of) the first Brillouin zone are indicated by thick (thin) lines. The nodal lines have C_{2y} rotation, inversion, and σ_y mirror symmetry. The vector q represents the CDW nesting vector to be considered in Sec. V, which is on the $k_x = 0$ plane. (b) Nodal lines projected onto the k_x - k_y plane. They intersect on the $k_x = 0$ line, owing to the C_{2y} rotational symmetry. (c) Fermi surface of HMTSF-TCNQ. Purple and green surfaces represent the electron and hole pockets, respectively. The Fermi surface consists of the alternating electron and hole pockets along the nodal lines.

A. Spin-lattice relaxation time T_1

The spin-lattice relaxation time T_1 reflects the electronic state near the Fermi level. To experimentally confirm the existence of nodal lines, we theoretically evaluate T_1 for the normal phase. Although there are several types of the origins

of spin-lattice relaxation, in this analysis we focus on the Fermi contact term between the conduction electron and the nucleus in each molecule, which is given by [49–51]

$$\frac{1}{(T_1)_\alpha} \propto T \int_{-\infty}^{\infty} [D_\alpha(\varepsilon)]^2 [-f'(\varepsilon)] d\varepsilon, \quad (10)$$

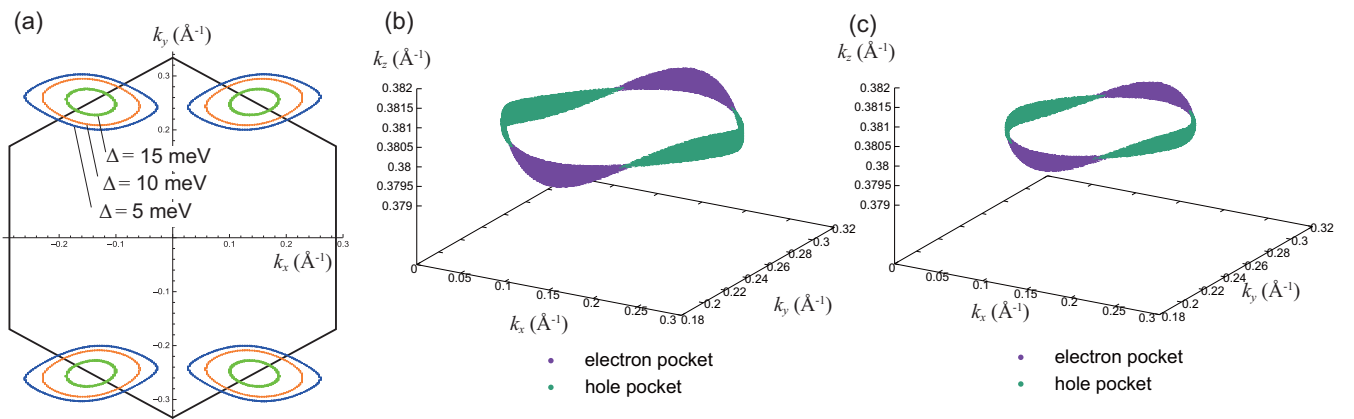


FIG. 7. (a) Projection of nodal lines onto the k_x - k_y plane for the CDW phase. The blue, orange, and green lines correspond to $\Delta = 5$, 10, and 15 meV, respectively. Electron and hole pockets for (b) $\Delta = 5$ meV and (c) $\Delta = 10$ meV. The purple and green surfaces represent the electron and hole pockets, respectively.

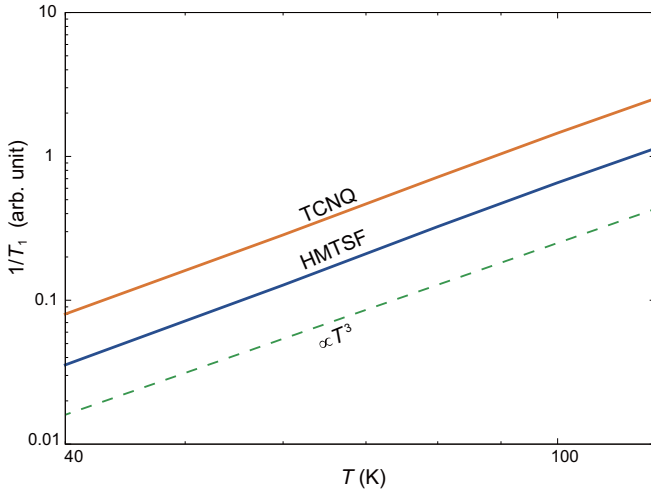


FIG. 8. Temperature dependence of $1/T_1$ above T_c . The blue and orange lines represent the theoretical values for the HMTSF and TCNQ molecules, respectively. The powers for the two molecules are approximately 3.1. The power T^3 is also indicated by a dashed line for reference.

where α indicates HMTSF or TCNQ, $D_\alpha(\varepsilon)$ is the DOS for the orbital α , and $f'(\varepsilon)$ is the derivative of the Fermi distribution function $f(\varepsilon) = [1 + e^{\beta(\varepsilon - \mu)}]^{-1}$. We assume that the chemical potential does not change with temperature above T_c . Figure 8 shows the temperature dependence of $1/T_1$ in the logscale without the CDW order parameter. The blue (orange) solid line represents the theoretical values evaluated by Eq. (10) for the HMTSF (TCNQ) molecule. The power T^3 is also shown for reference. We observe that $(T_1)_{\text{HMTSF}}$ and $(T_1)_{\text{TCNQ}}$ follow the power law $1/T_1 \propto T^{3.1}$, which is very close to the expected law $1/T_1 \propto T^3$ for pure two-dimensional Dirac electrons.

B. Orbital magnetic susceptibility

As mentioned in Sec. I, HMTSF-TCNQ shows a large diamagnetic susceptibility at low temperatures. To understand the origin and the temperature dependence, we evaluate the orbital magnetic susceptibility in the proposed model with nodal lines using the Fukuyama formula [29] given by

$$\chi_{\text{orbit}} = \frac{e^2}{\hbar^2} k_B T \sum_{nk} \text{Tr} \gamma_x \mathcal{G} \gamma_y \mathcal{G} \gamma_x \mathcal{G} \gamma_y \mathcal{G}, \quad (11)$$

where \mathcal{G} represents the thermal Green's function

$$\mathcal{G} = [i\varepsilon_n - H_{\text{CDW}}(\mathbf{k}) + \mu + i\Gamma \text{sgn}(\varepsilon_n)]^{-1}, \quad (12)$$

where $\varepsilon_n = (2n + 1)\pi k_B T$, Γ , and μ are the Matsubara frequency, the damping rate of the electron, and the chemical potential, respectively. γ_i is the current operator in the i ($= x$ or y) direction, which is defined by $\gamma_i = \partial H_{\text{CDW}}(\mathbf{k}) / \partial k_i$, and the n summation means the sum over the Matsubara frequency ε_n . The chemical potential is determined by the charge-neutrality condition

$$\sum_{lk} f(\varepsilon_{lk}) = \sum_{lk} [1 - f(\varepsilon_{lk})], \quad (13)$$

where ε_{lk} is the energy dispersion of the l th band.

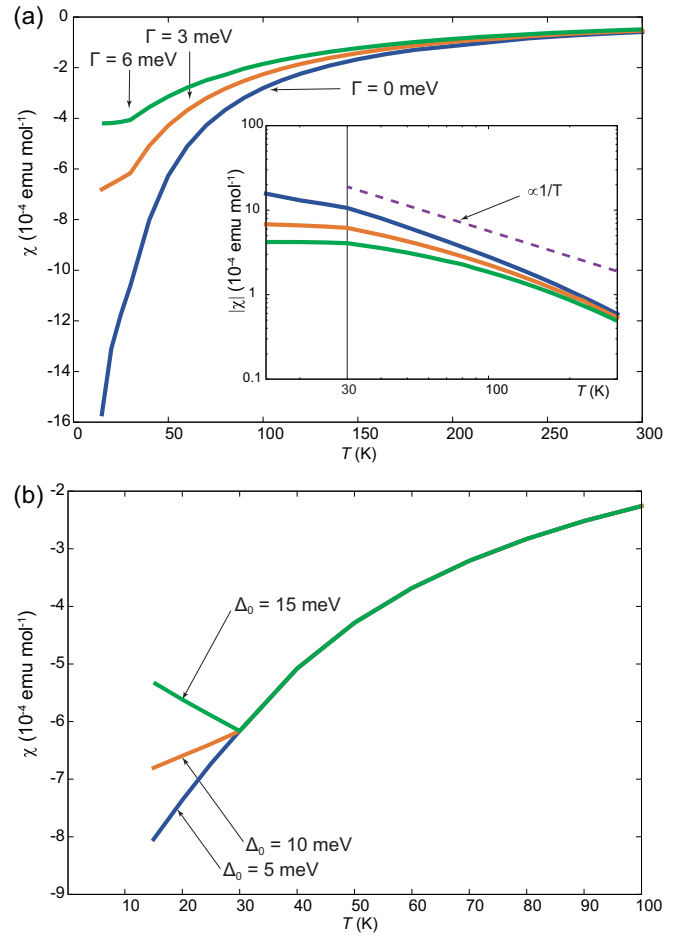


FIG. 9. (a) Orbital magnetic susceptibility for $\Delta_0 = 10$ meV as a function of the temperature. The blue, orange, and green lines correspond to $\Gamma = 0, 3,$ and 6 meV, respectively. Inset: Absolute value of the orbital magnetic susceptibility in the logscale. The power T^{-1} is also shown for reference. (b) Orbital magnetic susceptibility for $\Gamma = 3$ meV as a function of the temperature. The blue, orange, and green lines correspond to $\Delta_0 = 5, 10,$ and 15 meV, respectively.

For simplicity, we assume the temperature dependence of the order parameter, as typically used for the Bardeen-Cooper-Schrieffer superconductivity [52],

$$\Delta(T) = \Delta_0 \sqrt{1 - \frac{T}{T_c}}, \quad (14)$$

where Δ_0 is the order parameter at zero temperature. T_c is set to 30 K, which is in accordance with the experiment [53]. In the following analysis we evaluate the chemical potential by only considering the temperature dependence through Eq. (14) and setting $\beta \rightarrow \infty$ in Eq. (13). This approximation is justified when $T \simeq 0$; however, we expect that it is still valid at high temperatures because the thermal fluctuation overpowers the error of this approximation.

Integrating Eq. (11) numerically, we obtain the temperature dependence of the orbital magnetic susceptibility as shown in Fig. 9(a) for $\Delta_0 = 10$ meV ($\Gamma = 0, 3,$ and 6 meV). Above T_c

we observe that the orbital magnetic susceptibility increases negatively as the temperature decreases from the room temperature for every Γ . The nodal lines are the ensembles of Dirac electrons; therefore the Landau-Peierls contribution (the extension of the Landau diamagnetism to periodic systems) is expected to be very small [26,54], and the diamagnetism is attributed to the interband effect [22,23,26,27]. Interband diamagnetism in two-dimensional Dirac electrons has a temperature dependence of T^{-1} in the clean limit [55]. The inset of Fig. 9(a) indicates that the present numerical result for the $\Gamma = 0$ meV case (shown in blue) asymptotically obeys the power law for the low temperatures (~ 30 K). For the region $T_c < T < 100$ K, impurities affect the interband effect. Although the orbital magnetism in *massive* Dirac electron systems is not significantly sensitive to impurities [27], that in *massless* Dirac electrons is rather sensitive [23,24].

Below T_c we experience the effect of the nodal-line deformation as well as the interband effect and impurity scattering. The inflection at T_c is due to the order parameter. As the temperature decreases, the order parameter increases, the nodal lines shrink, and the diamagnetism is suppressed. We presume that the origins of this suppression to be decrease in the number and the reduction of velocities of the Dirac electrons. The relation between the magnitude of diamagnetism and detailed structure of nodal lines is discussed intensively in Ref. [56]. Note that a gap does not open in the DOS as long as $\Delta_0 < 18$ meV, and *massless* Dirac electrons are present for the cases shown in Fig. 9(a). Therefore, the diamagnetism diverges at zero temperature for the case of $\Gamma = 0$ meV, whereas the divergence is suppressed with a finite Γ .

Figure 9(b) shows the orbital magnetic susceptibility for the cases of $\Delta_0 = 5, 10,$ and 15 meV, where we set $\Gamma = 3$ meV as a typical value. For the case with a small Δ_0 , the diamagnetism monotonically increases as the temperature decreases. However, for the case with large Δ_0 , the nodal lines are strongly deformed, and the diamagnetism is suppressed rapidly. Whether χ_{orbit} decreases or increases as the temperature decreases depends on the following three effects: the interband effect, impurity scattering, and nodal-line deformation.

We compare the above theoretical results with a SQUID magnetometer measurement. The magnetizations were measured between 2–300 K using a SQUID magnetometer operated by a magnetic properties measurement system (Quantum Design Inc., CA, USA). A newly synthesized polycrystalline sample of ~ 5 mg is used. The core contribution of the diamagnetism estimated by Pascal's law (-2.8×10^{-4} emu/mol) is subtracted, as in the previous study [14]. The experimental data obtained in the cooling (heating) process are shown in Fig. 10 with circle (square) markers; the data reproduce the temperature dependence obtained in a previous study [14], including the absolute values.

Above 100 K, the total magnetic susceptibility is paramagnetic. However, as the temperature decreases, the diamagnetism prevails, and finally reaches a plateau below the CDW phase transition temperature, $T_c = 30$ K.

To understand the experimental results, we consider that the total magnetic susceptibility is given by

$$\chi_{\text{obs}} = a\chi_{\text{orbit}} + b\chi_{\text{Pauli}}, \quad (15)$$

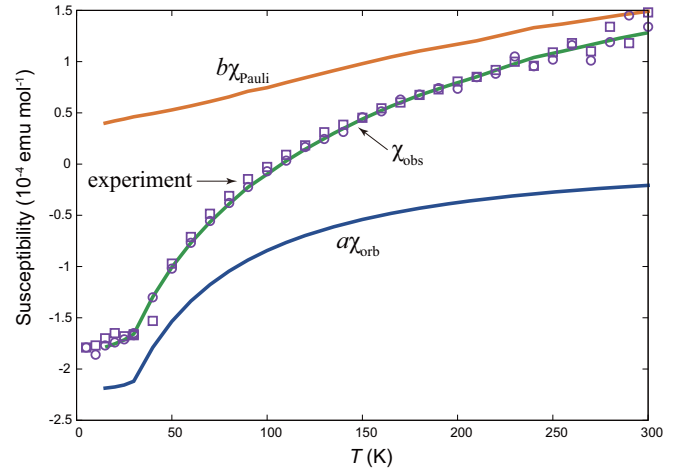


FIG. 10. Magnetic susceptibility as a function of temperature. The blue, orange, and green lines represent the theoretical evaluation of $a\chi_{\text{orbit}}$, $b\chi_{\text{Pauli}}$, and χ_{obs} , respectively, and the circle (square) markers represent the experimental data obtained by the SQUID magnetometer in the cooling (heating) process.

with positive coefficients a and b and χ_{Pauli} is the Pauli paramagnetic contribution

$$\chi_{\text{Pauli}} = -\mu_B^2 k_B T \sum_{nk} \text{Tr} \mathcal{G}^2, \quad (16)$$

where μ_B is the Bohr magneton $\mu_B = |e|\hbar/2m$. The coefficient a reflects the randomness of the polycrystal orientation, and it is expected to be smaller than 1 because χ_{orbit} is calculated under a magnetic field in the direction of the largest diamagnetism. However, the coefficient b ideally equals 1. Note that χ_{orbit} (χ_{Pauli}) is dominant at low (high) temperatures. Thus, the behavior below T_c is primarily determined by χ_{orbit} , which depends on Δ_0 and Γ up to a numerical factor. To reproduce the plateau that was experimentally observed, we choose $\Delta_0 = 11$ meV and $\Gamma = 4$ meV, and we set the numerical factor as $a = 0.4$. However, for the $T > 100$ K region, the dominant contribution is from $b\chi_{\text{Pauli}}$, and to fit the data, we set $b = 2.1$. We also show the obtained $a\chi_{\text{orbit}}$, $b\chi_{\text{Pauli}}$, and χ_{obs} in Fig. 10 with solid lines. The proposed theory is in excellent agreement with the experimental results for all temperature regions. This suggests that the experimental result is explained by the above scenario, i.e., the anomalous large diamagnetism at low temperatures is explained by the conflict between the interband effect, impurity scattering, and the deformation of nodal lines.

It should be noted that the coefficient b deviates from unity in this fitting. The origin of this deviation is not clear, however, it may be the intramolecular diamagnetism. Although this contribution has been partly subtracted as Pascal's law, a further consideration will be needed for a precise evaluation.

VII. CONCLUSION

The present study is based on a first-principles calculation and tight-binding analysis, and it predicts that an organic complex HMTSF-TCNQ is a new candidate material for the nodal-line semimetal. We have also clarified that the CDW

deforms open nodal lines into closed ones. We evaluated the spin-lattice relaxation time T_1 and the magnetic susceptibility. An experiment was also conducted to investigate the magnetization, and the large anomalous diamagnetism, the origin of which had long been controversial, was reproduced. The present theoretical evaluation of magnetic susceptibility is in excellent agreement with the experimental results, and it has clarified that the conflict between the interband diamagnetism, impurity scattering, and nodal-line deformation realizes this anomalous diamagnetism. Our evaluation of T_1 supports the existence of nodal lines, and it will be experimentally confirmed by means of a nuclear magnetic resonance measurement. This study is in progress, and the results will be presented elsewhere [33].

In the first-principles calculation we have neglected SOI. However, we expect that small SOI exists because of Se atoms. According to the indicator $(z_{2,2}, z'_2) = (1, 1)$, with SOI, all of the Dirac dispersions open gaps, and the system

TABLE III. Total energy calculated with different cutoffs.

Cutoffs	Total energy
$\{E_{wf}, E_\rho\} = \{70 \text{ Ry}, 320 \text{ Ry}\}$	-1519.72405531 Ry
$\{E_{wf}, E_\rho\} = \{140 \text{ Ry}, 640 \text{ Ry}\}$	-1519.75310850 Ry

will turn into a weak topological insulator [57]. Therefore, future work should focus on the electronic state and transport at the edge in the presence of SOI.

For this material, many intriguing physical properties besides the magnetic susceptibility have been investigated experimentally, e.g., the Seebeck coefficient and Hall conductivity. These properties are also expected to be derived from the interplay between the CDW and nodal lines. These characteristics will be elaborated by the framework proposed in this study.

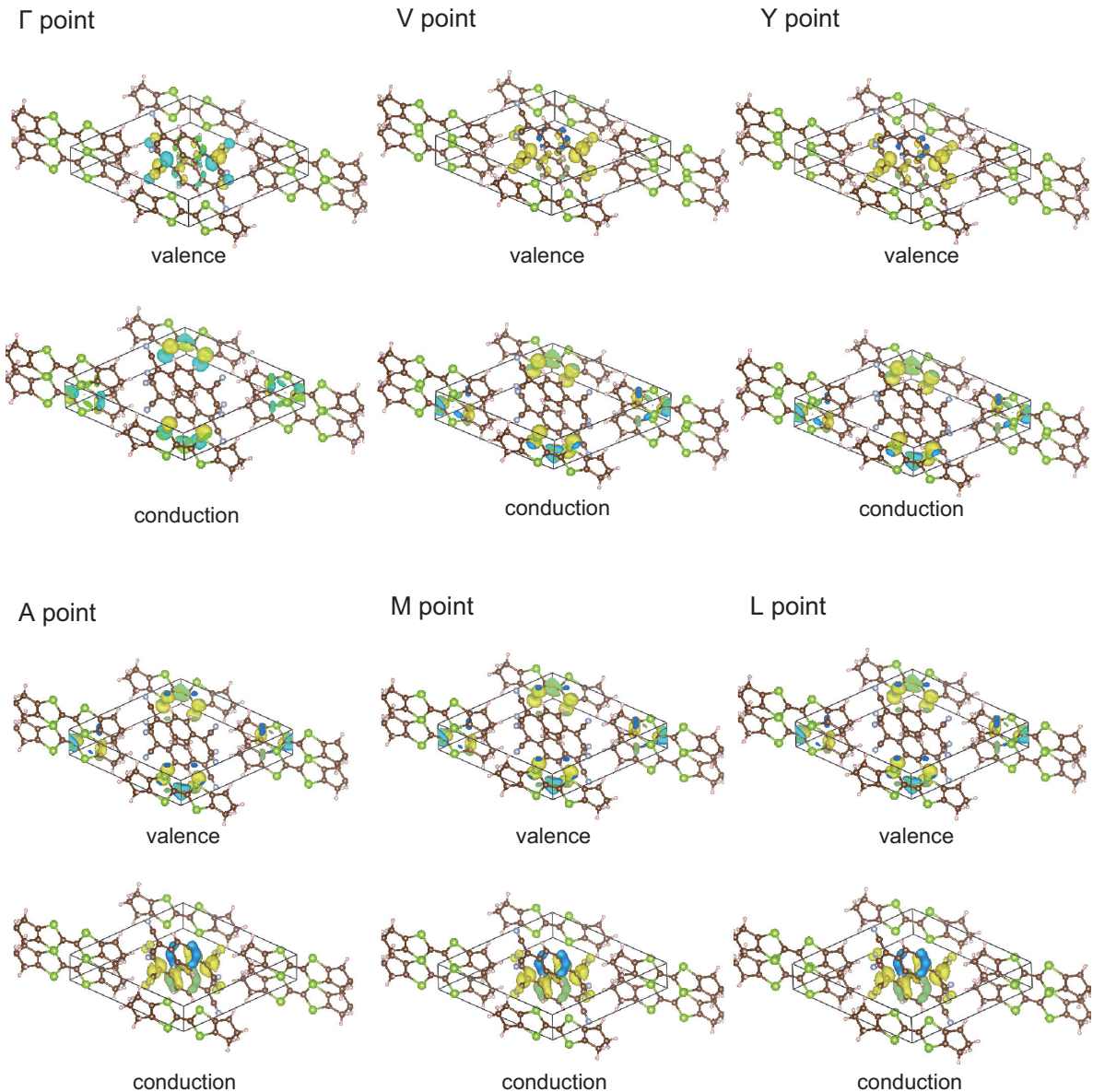


FIG. 11. Wave functions for the valence and conduction bands at the TRIM.

TABLE IV. Parities of inversion operation for the wave functions at TRIM.

	Γ	V	Y	A	M	L
Valence	+	-	+	-	+	+
Conduction	-	-	-	-	+	-

ACKNOWLEDGMENTS

We thank D. Miyafuji, T. Mizoguchi, M. Udagawa, H. Maebashi, H. Fukuyama, and M. Hirayama for fruitful discussions. We also thank R. Sugiura, T. Nakamura, and T. Takahashi for their magnetic susceptibility measurements, R. Kato for providing high quality samples, and H. Cui for providing crystal data. This work was supported by Grant-in-Aid for Scientific Research from the Japan Society for the Promotion of Science (Grants No. JP18H01162, No. JP19K03720, and No. JP18K03482). S.O. and I.T. were supported by the Japan Society for Science Promotion (JSPS) through the Program for Leading Graduate Schools (MERIT).

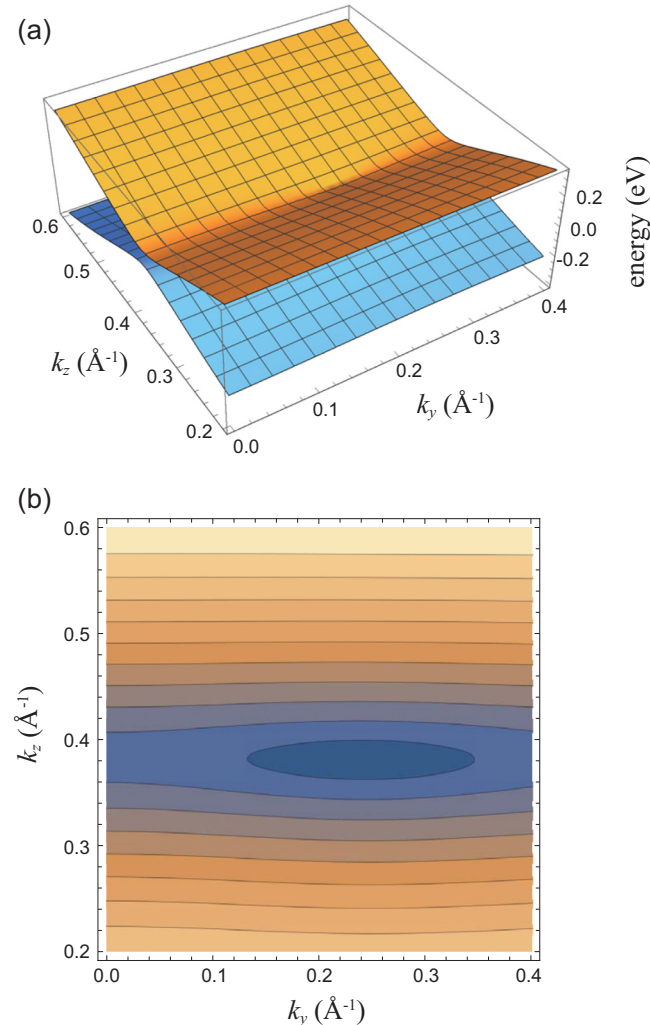


FIG. 12. (a) Energy dispersion near a Dirac point at $k_x = 0$. The orange (blue) surface corresponds to E_+ (E_-). (b) Contour plot of $E_+ - E_-$.

APPENDIX A: CUTOFF STABILITY OF THE FIRST-PRINCIPLES CALCULATION

We confirm the cutoff stability of the first-principles calculation by comparing the total energy calculated with different cutoffs E_{wf} and E_{ρ} , which are the cutoffs for the plane wave expansion and the electron density, respectively. The calculated total energy is tabulated in Table III between the cases of $\{E_{\text{wf}}, E_{\rho}\} = \{70 \text{ Ry}, 320 \text{ Ry}\}$ and $\{E_{\text{wf}}, E_{\rho}\} = \{140 \text{ Ry}, 640 \text{ Ry}\}$. These two values are close enough. Thus, we conclude that the first-principles calculation was performed properly.

APPENDIX B: WAVE FUNCTIONS AND INVERSION PARITIES AT TRIM

Figure 11 shows the wave functions for the valence and conduction bands at the TRIM, which are obtained by the

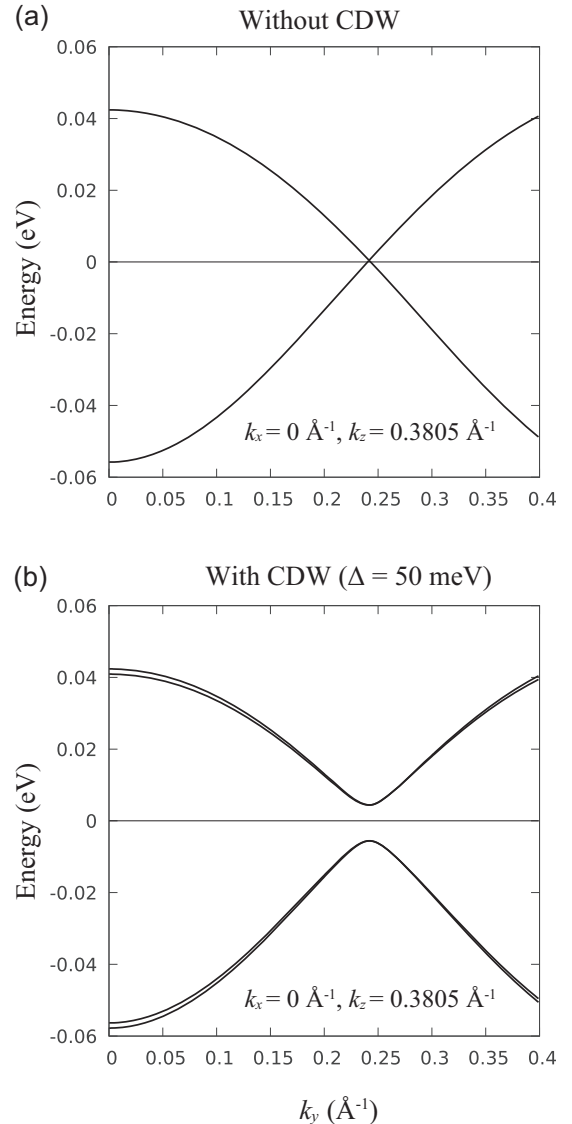


FIG. 13. Energy dispersion near a Dirac point at $k_x = 0 \text{ \AA}^{-1}$ and $k_z = 0.3805 \text{ \AA}^{-1}$ (a) without and (b) with a CDW with order parameter Δ . With a CDW, a gap of 2Δ opens at the gapless point.

first-principles calculation. For the Γ point, the colors in the figure represent the signs of the wave functions. For other k points, the wave functions are generally complex and are shown in yellow. The cross sections of the wave functions with the Brillouin zone boundary are shown in blue. Each wave function is the molecular orbital of either HMTSF or TCNQ. This suggests that the wave function at a generic point is also given by the linear combination of the wave functions for the two molecules, which justifies the assumption that the low-energy electronic state is described in terms of these two orbitals.

The parities of the inversion operation for the wave functions at TRIM are summarized in Table IV. The symmetry indicator is calculated from these values for the valence band.

APPENDIX C: DIRAC CONE

The energy dispersion near a Dirac point when $k_x = 0$ is shown in Fig. 12(a), and the contour plot of the difference of the energies $E_+ - E_-$ is shown in Fig. 12(b). We observe that the Dirac cone has strong anisotropy, and the system is two dimensional only in the vicinity of the Dirac point. The detailed energy dispersions are shown in Fig. 13(a) without CDW and Fig. 13(b) with CDW at $k_x = 0 \text{ \AA}^{-1}$ and $k_z = 0.3805 \text{ \AA}^{-1}$, which are obtained from the tight-binding model Eqs. (3) and (9), respectively. We observe the gapless energy dispersion without CDW, and the CDW opens a gap of 2Δ , which is the largest gap among the Dirac points on the nodal lines.

-
- [1] F. Qin, S. Li, Z. Z. Du, C. M. Wang, W. Zhang, D. Yu, H.-Z. Lu, and X. C. Xie, Theory for the Charge-Density-Wave Mechanism of 3D Quantum Hall Effect, *Phys. Rev. Lett.* **125**, 206601 (2020).
- [2] J. Gooth, B. Bradlyn, S. Honnali, C. Schindler, N. Kumar, J. Noky, Y. Qi, C. Shekhar, Y. Sun, Z. Wang, B. A. Bernevig, and C. Fleser, Axionic charge-density wave in the Weyl semimetal $(\text{TaSe}_4)_2\text{I}$, *Nature (London)* **575**, 315 (2019).
- [3] A. Kobayashi, S. Katayama, Y. Suzumura, and H. Fukuyama, Massless fermions in organic conductor, *J. Phys. Soc. Jpn.* **76**, 034711 (2007).
- [4] A. Kobayashi, Y. Suzumura, and H. Fukuyama, Hall effect and orbital diamagnetism in zero gap state of molecular conductor α -(BEDT-TTF) $_2\text{I}_3$, *J. Phys. Soc. Jpn.* **77**, 064718 (2008).
- [5] Z. F. Wang, Z. Liu, and F. Liu, Quantum Anomalous Hall Effect in 2D Organic Topological Insulators, *Phys. Rev. Lett.* **110**, 196801 (2013).
- [6] L. Z. Zhang, Z. F. Wang, B. Huang, B. Cui, Z. Wang, S. X. Du, H.-J. Gao, and F. Liu, Intrinsic two-dimensional organic topological insulators in metal-dicyanoanthracene lattices, *Nano Lett.* **16**, 2072 (2016).
- [7] Z. Liu, H. Wang, Z. F. Wang, J. Yang, and F. Liu, Pressure-induced organic topological nodal-line semimetal in the three-dimensional molecular crystal $\text{Pd}(\text{dddt})_2$, *Phys. Rev. B* **97**, 155138 (2018).
- [8] R. Kato, H. Cui, T. Tsumuraya, T. Miyazaki, and Y. Suzumura, Emergence of the Dirac electron system in a single-component molecular conductor under high pressure, *J. Am. Chem. Soc.* **139**, 1770 (2017).
- [9] R. Kato and Y. Suzumura, A tight-binding model of an ambient-pressure molecular Dirac electron system with open nodal lines, *J. Phys. Soc. Jpn.* **89**, 044713 (2020).
- [10] T. Kawamura, D. Ohki, B. Zhou, A. Kobayashi, and A. Kobayashi, Tight-binding model and electronic property of Dirac nodal line in single-component molecular conductor $[\text{Pt}(\text{dmdt})_2]$, *J. Phys. Soc. Jpn.* **89**, 074704 (2020).
- [11] R. Kato, H. Cui, T. Minamidate, H. H.-M. Yeung, and Y. Suzumura, Electronic structure of a single-component molecular conductor $[\text{Pd}(\text{dddt})_2]$ (dddt = 5, 6-dihydro-1, 4-dithiin-2, 3-dithiolate) under high pressure, *J. Phys. Soc. Jpn.* **89**, 124706 (2020).
- [12] A. N. Bloch, D. O. Cowan, K. Bechgaard, R. E. Pyle, R. H. Banks, and T. O. Poehler, Low-Temperature Metallic Behavior and Resistance Minimum in a New Quasi-One-Dimensional Organic Conductor, *Phys. Rev. Lett.* **34**, 1561 (1975).
- [13] K. Bechgaard, D. O. Cowan, and A. N. Bloch, Stabilization of the organic metallic state: The properties of two substituted tetraselenafulvalenes and their TCNQ salts, *Mol. Cryst. Liq. Cryst.* **32**, 227 (1976).
- [14] G. Soda, D. Jérôme, M. Weger, K. Bechgaard, and E. Pedersen, Spin relaxation and magnetic susceptibility studies of HMTSF-TCNQ, *Solid State Commun.* **20**, 107 (1976).
- [15] M. Weger, A model for the electronic band structure of HMTSeF-TCNQ, *Solid State Commun.* **19**, 1149 (1976).
- [16] K. Murata, Y. Fukumoto, K. Yokogawa, R. Takaoka, W. Kang, J. S. Brooks, D. Graf, H. Yoshino, T. Sasaki, and R. Kato, Magnetic-field-induced phase transitions in the quasi-one-dimensional organic conductor HMTSF-TCNQ, *Low Temp. Phys.* **40**, 371 (2014).
- [17] K. Murata, W. Kang, K. Masuda, T. Kuse, T. Sasaki, K. Yokogawa, H. Yoshino, J. S. Brooks, E. S. Choi, A. Kiswandhi, and R. Kato, Field-induced CDW in HMTSF-TCNQ, *Phys. B: Condens. Matter* **407**, 1927 (2012).
- [18] K. Murata, K. Yokogawa, K. Kobayashi, K. Masuda, T. Sasaki, Y. Seno, N. Rani Tamilselvan, H. Yoshino, J. S. Brooks, D. Jérôme, K. Bechgaard, M. Uruichi, K. Yakushi, Y. Nogami, and R. Kato, Field-induced successive phase transitions in the charge density wave organic conductor HMTSF-TCNQ, *J. Phys. Soc. Jpn.* **79**, 103702 (2010).
- [19] D. Jérôme and H. J. Schulz, Organic conductors and superconductors, *Adv. Phys.* **31**, 299 (1982).
- [20] D. Jérôme, Organic conductors: From charge density wave TTF TCNQ to superconducting $(\text{TMTSF})_2 \text{PF}_6$, *Chem. Rev.* **104**, 5565 (2004).
- [21] T. E. Phillips, T. J. Kistenmacher, A. N. Bloch, and D. O. Cowan, X-ray crystal structure of the organic conductor from 2, 2'-bi-(2,4-diselenabicyclo[3.3.0]octylidene) and 7, 7, 8, 8-tetracyano-p-quinodimethane (HMTSF-TCNQ), *J. Chem. Soc. Chem. Commun.* 334 (1976).
- [22] H. Fukuyama and R. Kubo, Interband effects on magnetic susceptibility. II. Diamagnetism of bismuth, *J. Phys. Soc. Jpn.* **28**, 570 (1970).
- [23] H. Fukuyama, Anomalous orbital magnetism and Hall effect of massless fermions in two dimension, *J. Phys. Soc. Jpn.* **76**, 043711 (2007).

- [24] M. Nakamura, Orbital magnetism and transport phenomena in two-dimensional Dirac fermions in a weak magnetic field, *Phys. Rev. B* **76**, 113301 (2007).
- [25] M. Koshino and T. Ando, Anomalous orbital magnetism in Dirac-electron systems: Role of pseudospin paramagnetism, *Phys. Rev. B* **81**, 195431 (2010).
- [26] A. Raoux, F. Piéchon, J. N. Fuchs, and G. Montambaux, Orbital magnetism in coupled-bands models, *Phys. Rev. B* **91**, 085120 (2015).
- [27] Y. Fuseya, M. Ogata, and H. Fukuyama, Transport properties and diamagnetism of Dirac electrons in bismuth, *J. Phys. Soc. Jpn.* **84**, 012001 (2015).
- [28] S. Ozaki and M. Ogata, Universal quantization of the magnetic susceptibility jump at a topological phase transition, *Phys. Rev. Res.* **3**, 013058 (2021).
- [29] H. Fukuyama, Theory of orbital magnetism of Bloch electrons: Coulomb interactions, *Prog. Theor. Phys.* **45**, 704 (1971).
- [30] K. Momma and F. Izumi, VESTA 3 for three-dimensional visualization of crystal, volumetric and morphology data, *J. Appl. Crystallogr.* **44**, 1272 (2011).
- [31] T. Hahn, U. Shmueli, and J. W. Arthur, *International Tables for Crystallography* (Reidel, Dordrecht, 1983), Vol. 1.
- [32] H. Cui and R. Kato (private communication).
- [33] K. Hiraki, H. Cui, and R. Kato (unpublished).
- [34] P. Giannozzi, S. Baroni, N. Bonini, M. Calandra, R. Car, C. Cavazzoni, D. Ceresoli, G. L. Chiarotti, M. Cococcioni, I. Dabo *et al.*, QUANTUM ESPRESSO: A modular and open-source software project for quantum simulations of materials, *J. Phys.: Condens. Matter* **21**, 395502 (2009).
- [35] P. Hohenberg and W. Kohn, Inhomogeneous electron gas, *Phys. Rev.* **136**, B864 (1964).
- [36] W. Kohn and L. J. Sham, Self-consistent equations including exchange and correlation effects, *Phys. Rev.* **140**, A1133 (1965).
- [37] J. P. Perdew, K. Burke, and M. Ernzerhof, Generalized Gradient Approximation Made Simple, *Phys. Rev. Lett* **77**, 3865 (1996).
- [38] L. Fu and C. L. Kane, Topological insulators with inversion symmetry, *Phys. Rev. B* **76**, 045302 (2007).
- [39] H. Po, A. Vishwanath, and H. Watanabe, Symmetry-based indicators of band topology in the 230 space groups, *Nat. Commun.* **8**, 50 (2017).
- [40] Z. Song, T. Zhang, Z. Fang, and C. Fang, Quantitative mappings between symmetry and topology in solids, *Nat. Commun.* **9**, 3530 (2018).
- [41] Y. Kim, B. J. Wieder, C. L. Kane, and A. M. Rappe, Dirac Line Nodes in Inversion-Symmetric Crystals, *Phys. Rev. Lett.* **115**, 036806 (2015).
- [42] Z. Song, T. Zhang, and C. Fang, Diagnosis for Nonmagnetic Topological Semimetals in the Absence of Spin-Orbital Coupling, *Phys. Rev. X* **8**, 031069 (2018).
- [43] J. C. Slater and G. F. Koster, Simplified LCAO method for the periodic potential problem, *Phys. Rev.* **94**, 1498 (1954).
- [44] A. A. Mostofi, J. R. Yates, G. Pizzi, Y.-S. Lee, I. Souza, D. Vanderbilt, and N. Marzari, An updated version of WANNIER90: A tool for obtaining maximally-localised Wannier functions, *Comput. Phys. Commun.* **185**, 2309 (2014).
- [45] S. Ravy, P. Launois, R. Moret, and J.-P. Pouget, Case studies of molecular disorder, *Z. Kristallogr.* **220**, 1059 (2005).
- [46] H. Fröhlich, On the theory of superconductivity: The one-dimensional case, *Proc. R. Soc. London Ser. A* **223**, 296 (1954).
- [47] C. G. Kuper, The thermal decomposition of ammonium perchlorate II. The kinetics of the decomposition, the effect of particle size, and discussion of results, *Proc. R. Soc. London Ser. A* **227**, 214 (1955).
- [48] M. J. Rice and S. Strässler, Theory of a quasi-one-dimensional band-conductor, *Solid State Commun.* **13**, 125 (1973).
- [49] T. Moriya, The effect of electron-electron interaction on the nuclear spin relaxation in metals, *J. Phys. Soc. Jpn.* **18**, 516 (1963).
- [50] Y. Suzumura, NMR relaxation rate of impure anisotropic quasi-one-dimensional superconductors, *J. Phys. Soc. Jpn.* **58**, 2642 (1989).
- [51] S. Katayama, A. Kobayashi, and Y. Suzumura, Electronic properties close to Dirac cone in two-dimensional organic conductor α -(BEDT-TTF)₂I₃, *Eur. Phys. J. B* **67**, 139 (2009).
- [52] A. L. Fetter and J. D. Walecka, *Quantum Theory of Many-Particle Systems* (Dover, New York, 2003).
- [53] J. Cooper, M. Weger, D. Jérôme, D. Lefur, K. Bechgaard, A. Bloch, and D. Cowan, Semi-metallic behaviour of HMTSF-TCNQ at low temperatures under pressure, *Solid State Commun.* **19**, 749 (1976).
- [54] M. Ogata, Orbital magnetism of Bloch electrons: III. application to graphene, *J. Phys. Soc. Jpn.* **85**, 104708 (2016).
- [55] J. W. McClure, Diamagnetism of graphite, *Phys. Rev.* **104**, 666 (1956).
- [56] I. Tateishi, V. Könye, H. Matsuura, and M. Ogata, Characteristic singular behaviors of nodal-line materials emerging in orbital magnetic susceptibility and Hall conductivity, *Phys. Rev. B* **104**, 035113 (2021).
- [57] L. Fu, C. L. Kane, and E. J. Mele, Topological Insulators in Three Dimensions, *Phys. Rev. Lett.* **98**, 106803 (2007).